Nanoscale

On the Structure and Chemistry of Iron Oxide Cores in Human Heart and Human Spleen Ferritins using Graphene Liquid Cell Electron Microscopy

Journal:	*Nanoscale*
Manuscript ID	NR-ART-02-2019-001541.R2
Article Type:	Paper
Date Submitted by the Author:	14-Aug-2019
Complete List of Authors:	Narayanan, Surya; University of Illinois at Chicago, Department of Bioengineering Firlar, Emre; University of Illinois at Chicago, Department of Bioengineering; University of Illinois at Chicago, Department of Mechanical and Industrial Engineering Rasul, Md Golam; University of Illinois at Chicago, Department of Mechanical and Industrial Engineering Foroozan, Tara; University of Illinois at Chicago Farajpour, Nasim; University of Illinois at Chicago, Department of Electrical and Computer Engineering, Chicago IL, 60607, USA Covnot, Leigha; University of Illinois at Chicago, Department of Bioengineering Shahbazian-Yassar, Reza; University of Illinois at Chicago, Mechanical and Industrial Engineering; University of Illinois at Chicago Shokuhfar, Tolou; University of Illinois at Chicago, Department of Bioengineering; Michigan Technological University, Department of Mechanical Engineering

Journal Name

ARTICLE

On the Structure and Chemistry of Iron Oxide Cores in Human Heart and Human Spleen Ferritins using Graphene Liquid Cell Electron Microscopy

Sample Received 00th January 20xx,
Accepted 00th January 20xx

DOI: 10.1039/x0xx00000x

www.rsc.org/

Surya Narayanan[a, &], Emre Firlar[a,b,&], Md Golam Rasul[b], Tara Foroozan[b], Nasim Farajpour[c], Leigha Covnot[a], Reza Shahbazian-Yassar[b*], and Tolou Shokuhfar[a*]

Ferritin is a protein that regulates the iron ions in humans by storing them in the form of iron oxides. Despite extensive efforts to understand the ferritin iron oxide structures, it is still not clear how ferritin proteins with distinct light (L) and heavy (H) chain subunit ratio impact the biomineralization process. *In situ* graphene liquid cell-transmission electron microscopy (GLC-TEM) provides an indispensable platform to study the atomic structure of ferritin mineral cores in their native liquid environment. In this study, we report differences in the iron oxide formation in human spleen ferritins (HSFs) and human heart ferritins (HHFs) using *in situ* GLC-TEM. Scanning transmission electron microscopy (STEM) along with selected area electron diffraction (SAED) of the mineral core and electron energy loss spectroscopy (EELS) analyses enabled the visualization of morphologies, crystal structures and the chemistry of iron oxide cores in HSFs and HHFs. Our study revealed the presence of metastable ferrihydrite ($5Fe_2O_3.9H_2O$) as a dominant phase in hydrated HSF and HHF, while stable hematite (α-Fe_2O_3) phase predominated in non-hydrated HSFs and HHFs. In addition, higher Fe^{3+}/Fe^{2+} ratio in HHFs was found in comparison to HSFs. This study provides new understanding on iron-oxide phases that exist in hydrated ferritin proteins from different human organs. Such new insights are needed to map ferritin biomineralization pathways and possible correlations with various iron-related disorders in human.

[a] *University of Illinois at Chicago, Department of Bioengineering, Chicago IL, 60607, USA*
[b] *University of Illinois at Chicago, Department of Mechanical and Industrial Engineering, Chicago IL, 60607, USA.*
[c] *University of Illinois at Chicago, Department of Electrical and Computer Engineering, Chicago IL, 60607, USA*
& Equal Contribution; co- first authors
**Corresponding authors*
†Electronic Supplementary Information (ESI) available: [details of any supplementary information available should be included here]. See DOI: 10.1039/x0xx00000x

Introduction

Ferritins are globular protein shells with an 8 nm cavity inside capable of storing few thousands of iron ions to form iron oxide core crystal structures.[1] In order to better understand the mineral core structure and kinetics involved in iron regulation, many groups employed bulk characterization techniques such as X-ray diffraction (XRD)[2], Mossbauer spectroscopy[3], small angle X-ray scattering (SAXS)[4], X-ray near edge spectroscopy (XANES)[4], superconducting quantum interference device (SQUID)[4], and X-ray absorption spectroscopy (XAS).[5] These techniques, however, lack sufficient spatial resolution to probe the local chemistry and atomic order at the scale of individual ferritin proteins particularly within liquid environment.[6]

Transmission electron microscopy (TEM) is a powerful characterization technique to study the structure and chemistry of iron mineral core of ferritin at nanoscale.[4,7–12] Most studies of ferritin structure have been performed in non-hydrated state where the ferritins were dried before imaging in TEM. Based on the electron nanodiffraction studies[8,13] and high-resolution transmission electron microscopy (HRTEM)[8] of physiological horse spleen ferritins (HoSFs)[8,13], human liver ferritins (HLF)[8], and human brain ferritins (HBF)[8], it was reported that all the ferritin types are composed of major phases of hexagonal 6-line ferrihydrite (6LFh) and hematite, with traces of magnetite (Fe_3O_4) or maghemite (γ-Fe_2O_3).[8,13] Conversely, pathological ferritin from HBF indicated minor phases of 6LFh and absence of hematite, however the dominant phase was cubic magnetite[8]. Further, based on HRTEM[14], electron energy loss spectroscopy (EELS)[14], and microdiffraction studies[15], Quintana *et al.*, reported that the crystal structure of physiological HoSF exhibited 6LFh[14] and hematite as a major phase[15].In contrast, pathological HBF was composed of major phases of magnetite and traces of ferrihydrite[14]. They also observed highly disordered stacking of oxygen and iron ions.[8] Galvez *et al.* also observed HoSF exhibiting different iron oxide phases during the stages of demineralization process.[4] It is interesting to note that the composition of each phases of iron oxide was dependent on the stages of iron removal.[4]

On contrary to the results reported by Cowley *et al*.[13], Quaintana *et al.* [8,14,15] and Galvez *et al*.[4], Pan and his co-workers showed that the iron core in HLF is made of single iron oxide phase 6LFh[9]. Through several[10,16,17] electron beam irradiation experiments on human liver biopsy, it was shown that under intense electron beam, iron oxide transformations might occur due to the shift of Fe^{3+} ions from octahedral coordinated sites to tetrahedral sites[16]. It was concluded that the earlier observation of magnetite/maghemite phases might be a consequence of electron beam irradiation[9].

While the studies discussed thus far have improved the understanding of the structural aspects in ferritin proteins, the reported results are not consistent. The ambiguities surrounding iron core oxide phases, composition, and their relationship to the protein molecular structure calls for more detailed investigation of ferritin proteins in their native state. The small size of iron core and the difficulties associated with imaging of ferritin in its native hydrated environment might pose difficulties in understanding the iron oxide composition in ferritin.

With conventional protein specimen preparation for electron microscopy, artifacts could be introduced.[18] The evolution of electron cryomicroscopy (CryoEM) enabled the visualization of ferritin in frozen state[19], however, it has major limitation to capture the dynamics of biomineralization pathways. The development of microfluidic-based liquid cell enclosures with Si_3N_4 membranes for TEMs has opened a new era to study biological structures.[20] This development enabled to resolve structural features and dynamics of COS-7 cells[21], tumor cells[22], yeast cells[23], and other biological materials.[24,25] Furthermore, dynamic TEM (dTEM) was coupled with *in situ* Si_3N_4 based liquid microscopy to improve the spatial and temporal resolution, such that the conformational dynamics of the ferritin proteins could be observed.[26] While the dTEM technique has inheritably low resolution, it should be noted that the thickness of Si_3N_4 membrane makes it difficult to obtain lattice resolution images of the iron-oxide mineral cores within ferritins.[27]

On the other hand, graphene-liquid cell (GLC) has revolutionized our ability to resolve the atomic structure and chemistry at unprecedented resolutions. Yuk *et al.* developed this technique and observed the dynamics of Pt nanoparticles growth.[28] Further, Wang *et al.* pioneered the atomic resolution characterization of HoSF in GLCs[18] and the precise control of electron beam to induce hydrogen molecule formation during GLC-scanning TEM (STEM) studies.[29] The superb electrical conductivity of graphene and its ability to scavenge free radicals make it a suitable candidate to image and analyse radiation sensitive biological materials in their native liquid environment.[30]

As reported in our earlier study on HoSF, the chemical signature of iron oxide core in hydrated ferritin

proteins is significantly different than the ferritins in non-hydrated state. In particular, the EELS study from hydrated HoSF ferritin showed higher ratios of Fe^{2+}/Fe^{3+} in the mineral core as compared to the non-hydrated ferritins.[18] As such, it is important to investigate the iron core of ferritins in their native environment. Herein, we utilized GLC-STEM to characterize the iron oxide core minerals in in different organ ferritins (human heart and human spleen) with varying ratios of heavy (H) and light (L) subunits. Through high angle-annular dark field (HAADF)-STEM imaging, the size and morphological characteristics of HSF and HHF were determined. The SAED and HRTEM analyses enabled the characterization of the crystal structure of HSF and HHF proteins. Furthermore, via the Fe $L_{2,3}$ edge analysis, the relative Fe^{3+}/Fe^{2+} ratio in the iron oxide cores of HSF and HHF in GLC were compared.

Results and Discussion

Morphology and Size of Ferritins:

The morphology and the size differences of HSFs and HHFs are shown in Figure 1. Figure 1A shows the HAADF-STEM image collected from HSFs in GLC exhibiting different morphologies with geometric and non-geometric shapes. The magnified images of the four particularly observed morphologies are depicted in Figure 1B with their corresponding schematics: (i) full spherical, (ii) doughnut, (iii) trigonal pyramid, and (iv) crescent shapes. A similar trend was also observed in the HAADF-STEM images collected from HHFs as shown in Figure 1C. Different morphologies observed in HHFs are also reported in the schematics along with the magnified images in Figure 1D. In addition to the stick and boot like morphology that was discussed earlier by López-Castro *et al.*[31], small spherical, bow-tie, crescent, and spherical morphologies were also observed in our work. Possible reasons can explain these different morphologies. (a) Periodic arrangement of iron crystals and stacking of various mineral core in different sites and direction within the inner layer of the protein contribute to cubic symmetry.[1,32] Further, the random orientation of the proteins on the support membrane results in different morphologies.[9](b) The protein's inner architecture might dictate the growth of the iron oxide core thus exhibiting different morphologies.[33](c) The nucleation sites, controlled by the number and positioning of the eight hydrophilic three fold symmetry channels determine the differences in morphology.[9] This theory is also supported by a model, called as 24-n nucleation model, which describes the differences in the nucleation sites in HSFs and HHFs.[31] (d) The number of iron ions that enter the protein during the distinct stages of biomineralization, and the availability of iron ions for nucleation might contribute to different morphologies in HSFs and HHFs.[9,4,34]

In addition to the above mentioned points, it is suggested that in a native form, both HSFs and HHFs can have different distribution of H and L subunits.[1] The position and the number of H and L subunits might also have an impact on the morphologies that are exhibited in both HSFs and HHFs. In this study, HSFs were obtained from native source while HHFs were obtained from a recombinant ferritin source. While a naturally available source of protein can exhibit different ratios of H/L subunits, studies have shown that the ratio of H and L subunits can be controlled in a recombinant protein structure.[35] Due to these differences in the source of protein, the number of morphologies that are observed in HHFs could be limited. Future studies can consider using HHF from a native source to discover some unique morphologies that are not reported in this work. Furthermore, it is shown that higher ratios of H/L subunits has influence on the number of iron that enters the ferritin to form iron oxide core, as well as the kinetics of biomineralization and demineralization.[35] Previous study showed that with fewer number of ferroxidase sites and slower oxidation rates, L rich ferritins tend to have bigger iron oxide core with more pronounced crysallinity.[35] Figure 1E represents the iron oxide core size distributions of HSF and HHF. The graph represents a bell curve of 150 different iron oxide cores for HSFs and HHFs with a similar particle size distribution. Since the iron oxide core shape is not spherical, area was considered for the size comparison. The average size distribution of HSFs was found to be 26 ± 9 nm^2 while this for HHFs was slightly lower (24 ± 8 nm^2). One reason behind that could be the slow mineralization in the L subunit rich ferritins, HSF, as it is also reported in the literature.[36]The area of iron oxide core within ferritins was analyzed based on the morphologies as shown in Figure 1F. The bar chart represents the area (black color) and frequency (red color) of HSFs and HHFs. HSFs displayed higher frequency of spherical (32.5 ± 10.8 nm^2) morphologies as compared to the crescent (19.48 ± 5.8 nm^2), trigonal pyramid (21.74 ± 5.8 nm^2), and doughnut (32.97 ± 2.3 nm^2) morphologies. On the other hand, the distribution of crescent (18.75 ± 4.4 nm^2), small spherical (18.47 ± 4.2 nm^2), bow-tie (26.72 ± 3.88 nm^2), and spherical (35.34 ± 4.5 nm^2) morphologies in HHF did not follow a trend. The frequency of occurrence of different morphologies might be a representation of different stages of biomineralization.[9] There is also a possibility that it indicates the role of H and L subunits in HSF and HHF during

the nucleation and growth of the minerals.[31] It should be noted that the sample dataset is not comparable with the ones used typically in the cryo-EM community. Considering the randomness of graphene liquid pockets across the grid, it is challenging to incorporate high-throughput automated data collection system to collect large datasets.

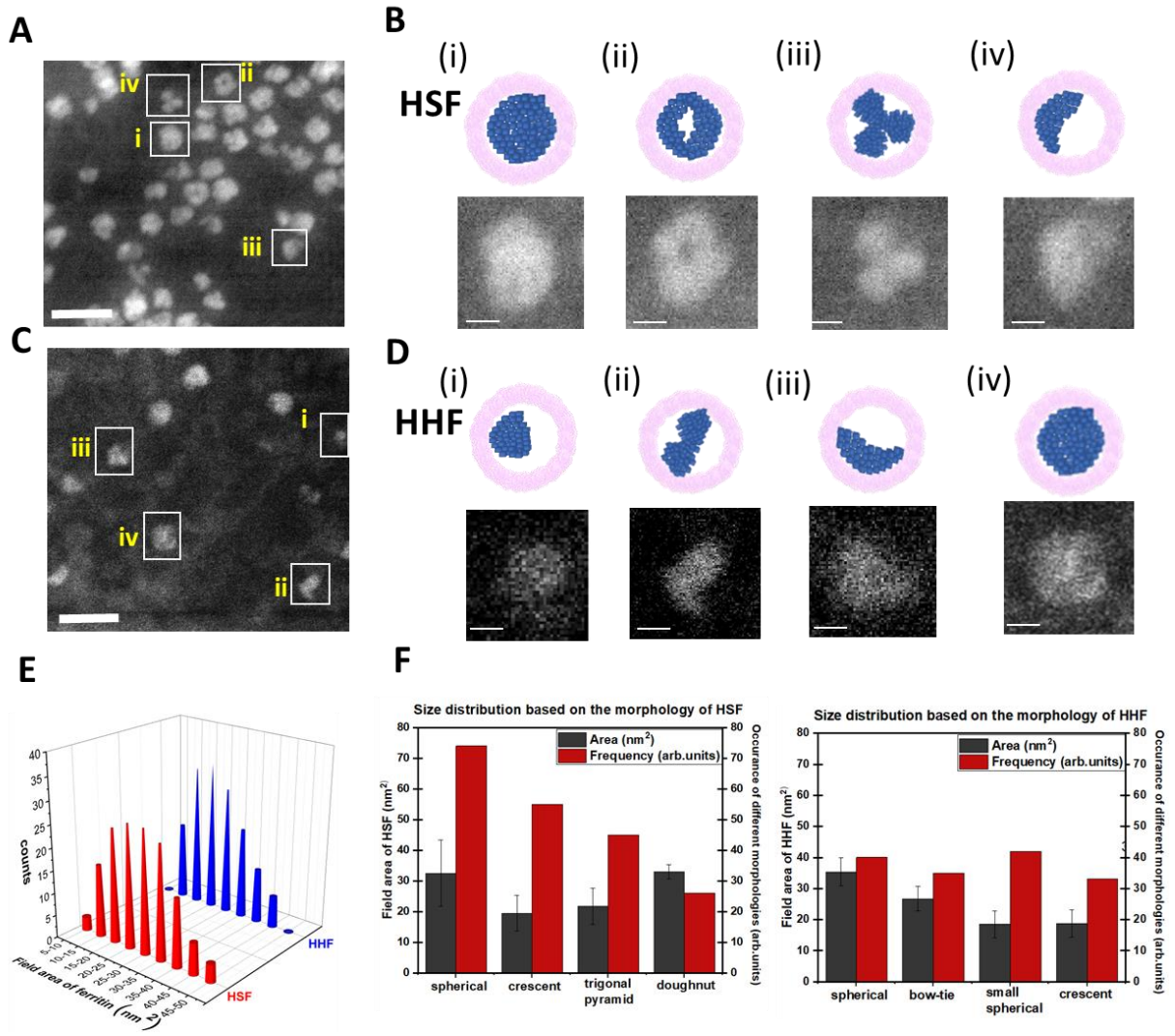

Figure 1. Morphological characterization of HSF and HHF proteins in GLCs. A. HAADF-STEM image of HSF in GLC showing different morphologies with geometric and non-geometric shapes (Scale bar: 20 nm). **B.** Magnified images of different geometric morphologies observed in **A** and their corresponding schematics representing the morphologies that are exhibited by HSF. The different morphologies depicted are: (i) full spherical; (ii) doughnut; (iii) trigonal pyramid; and (iv) crescent. (Scale bars: 2 nm). The pink color represents the protein shell while the blue color represents the iron oxide core in ferritin. **C.** The HAADF-STEM image of HHF in GLC showing different morphologies with geometric and non-geometric shapes (Scale bar: 20nm). **D.** Magnified images of different geometric morphologies observed in Figure **C** and their corresponding schematics representing the morphologies that are exhibited by HHF: (i) small spherical; (ii) bow-tie; (iii) crescent; and (iv) spherical. (Scale bars: 2 nm). The pink color represents the protein shell while the blue color represents the iron oxide core in ferritin. **E.** Size distribution of iron cores in HHF and HSF proteins based on the area of the particles in the HAADF-STEM images. The size distribution measurements showed 26 $\pm$ 9 nm^2 for HSF and 24 $\pm$ 8 nm^2 for HHF (n=150 for each type of ferritin). **F.** The size distribution measurements of HSF

and HHF (n=150 for each type of ferritin) with respect to different morphologies in HSF and HHF. This work focuses on the morphologies with geometrical shapes.

Structural Characterization of Ferritins

Figure 2 represents the structural characterization of HSFs and HHFs using SAED and high resolution TEM (HR-TEM) techniques. The SAED analysis (n>6 for both type of ferritins) were carried out to determine the average crystal structure of many different ferritin cores from a selected area in liquid state, while HR-TEM was employed to monitor the crystal structure of individual protein mineral cores in the non-hydrated state. Figure 2A shows both the reference TEM image and SAED collected from an area where multiple HSF particles are present. The *d* spacings of 3.5, 3.1, 1.9, 1.7, 1.5, and 1.1 Å indicate the presence of hematite (H), ferrihydrite (Fh), and traces of goethite or magnetite with planes of H(012), M(220)/G(020), Fh(113), Fh(114), Fh(115) and H(128), respectively. Quintana *et al.* also showed the presence of ferrihydrite and hematite for HSF through dry state HR-TEM.[8] Figure 2B, on the other hand, represents the reference TEM image and SAED collected from an area where multiple HHF particles are present. SAED pattern showed *d* spacings of 3.0, 2.2, 2.0, 1.8, and 1.6 Å, which indicate the presence of hematite, ferrihydrite, and traces of magnetite or maghemite with the planes of M(220)/MH(220), Fh(112) or H(113), Fh(113), H(024), and H(116) or MH(511), respectively.

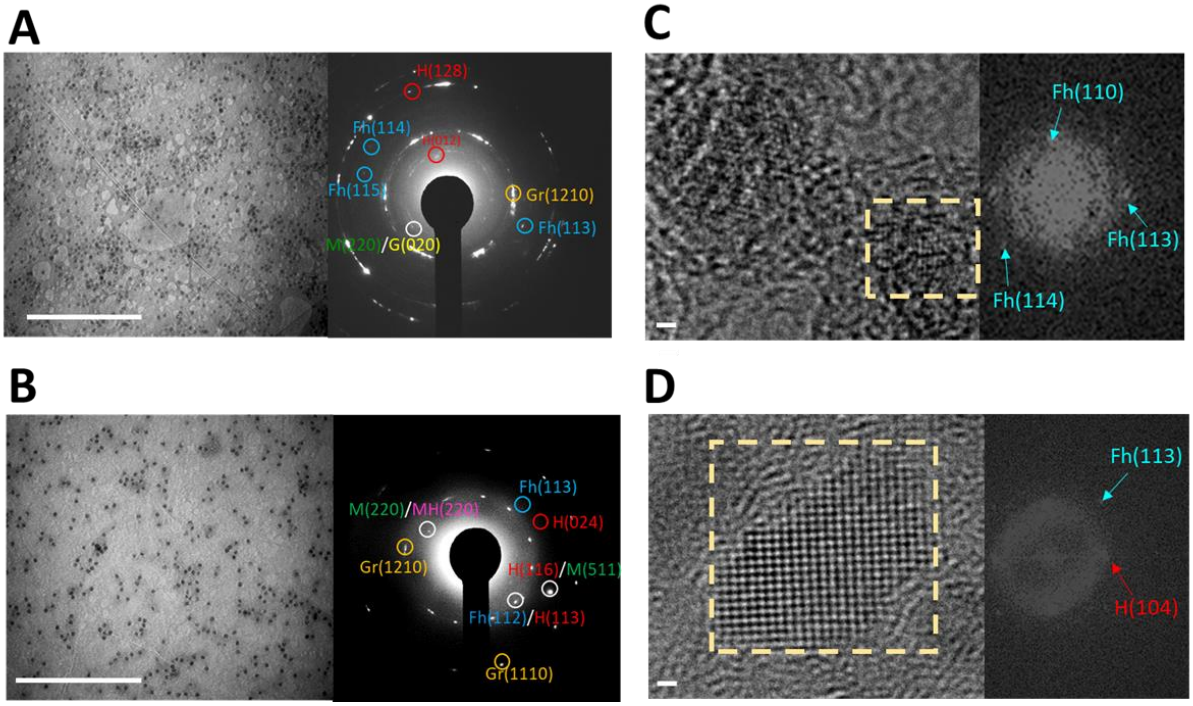

Figure 2. Electron microscopy characterization of HSF and HHF proteins. A. TEM image and the corresponding SAED of HSF indicate d spacings of 3.5, 3.1 ,1.9 ,1.7, 1.5 and 1.1 Å representing crystal structures with planes H(012), M(220) or G(020), Fh (113), Fh(114), Fh(115) and H(128), respectively. The d spacings of graphene of 1.2 Å is represented as Gr(1210) **B**. TEM image and the corresponding SAED of HHF indicate *d* spacings of 3.0, 2.2, 2.0, 1.8, and 1.6 Å representing crystal structures with planes M(220) or MH(220), Fh(112) or H(113), Fh(113), H(024), and H(116) or M(511), respectively. The *d* spacings of 2.1 and 1.2 Å represents Gr(1100) and Gr(1210), respectively. Green, blue, yellow, red, pink and gold colors in the SAED represent magnetite (M), ferrihydrite (Fh), goethite (G), hematite (H), maghemite (MH) and graphene, respectively. Scale bars of the TEM images in A and B are 100nm. **C**. HR-TEM image of HSF with the FFT obtained from the dashed square (yellow color) area of the image. Interplanar spacings of 2.4, 1.97, and 1.49 Å in the FFT refer to (110), (114) and (113) planes of ferrihydrite, respectively. **D**. HR-TEM image of HHF with the FFT obtained from the dashed square (yellow color) area of the image. Interplanar spacings of 2.7 and 1.9 Å in the FFT refer to (104) plane of hematite and (113) plane of ferrihydrite, respectively. Scale bars of HR-TEM images in C and D are 2 nm.

Considering these, HSF and HHF showed similar crystal structures indicating the presence of ferrihydrite as a predominant phase along with hematite. In addition to that, some of the d spacings from HSF also matched with the planes of magnetite as well as goethite. On the other hand, HHF indicated trace amounts of magnetite/ maghemite. To be able to study the individual crystal structures, furthermore, HR-TEM images were collected from HSF and HHF and presented in Figure 2C and 2D, respectively. Their corresponding Fast Fourier Transforms (FFT) showed interplanar spacings of 2.4, 1.97, and 1.49 Å representing ferrihydrite with planes (110), (114) and (113) for HSF, respectively, in Figure 2C, and 2.7, and 1.9 Å representing hematite with plane (104) and ferrihydrite with plane (113) for HHF, respectively, in Figure 2D.[37] HR-TEM does not represent all the iron oxide minerals reported via SAED because not all the crystals in the mineral core are in the right crystallographic zone axis. Hence, the planes of goethite, magnetite, and hematite were not observed in HSF. Likewise, planes of maghemite, and magnetite was not observed in HHF from the HR-TEM images

Chemical Characterization of Ferritins

The ability to acquire EELS maps at 10^6 $e^-/Å^{-2}/s$ has showcased the ability of graphene to maintain the integrity of protein structure in ferritin during high dose EELS signals collection.[18] In this work, the differences in the chemical composition of the mineral cores in HSF and HHF in their native state are investigated via GLC-STEM-EELS. White line analysis on iron L_3 and L_2 core edges was implemented for the determination of oxidation state of transition metals.[42,40] It was reported that with the increasing area integral ratio of L_3 to L_2, oxygen to transition metal ratio increases.[39] This technique was also employed here to determine the relative ratio of O to Fe, which, in turn, also indicates the variation in the Fe^{3+} to Fe^{2+} ratio. Figure 3A represents the iron L_3 and L_2 edges obtained from HSF and HHF (n= 3 for both the ferritin types). Comparing the integral intensities under these white lines, the L_3/L_2 ratios are 4.24 ± 0.06 for HSF and 4.53 ± 0.04 for HHF, as shown in Figure 3B. These results were compared with the magnetite and hematite standards which indicated that as this ratio increases, the ratio of O/Fe or Fe^{3+}/Fe^{2+} increases.[40]

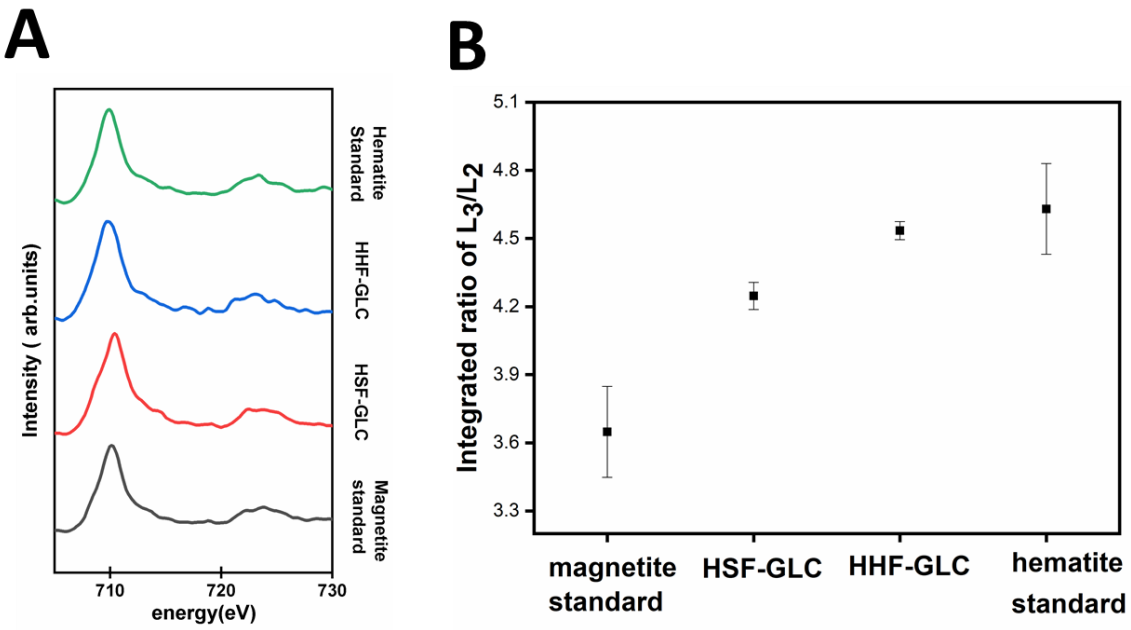

Figure 3. Chemical Characterization of HSF and HHF via GLC-STEM-EELS. Chemical characterization of HSF and HHF. **A**. STEM-EELS in GLC shows the comparison of Fe $L_{2,3}$ edges in HSF and HHF iron cores with the iron oxide standards. **B.** Relative area integral ratio of $L_3$to L_2 Fe edges in HSF and HHF. The higher ratios in HHF (4.53±0.04) as compared to HSF (4.24±0.06) indicates

higher O to Fe ratio, that is, presence of higher Fe^{+3} / Fe^{+2} in HHF as compared to HSF (n=3 for both the ferritin types). Magnetite (3.64 ± 0.2) and hematite (4.63 ± 0.2) standards (n=3) are represented to draw an understanding of the Fe^{3+} /Fe^{2+} ratio.

Schematic 1 represents the differences in the iron oxide composition in HSF and HHF based on our observation reported here. Diffraction patterns from hydrated HSFs and HHFs indicated higher amount of ferrihydrite in comparison to other phases of iron oxide in both HSFs and HHFs. In addition to that, some amount of hematite was observed in both the organ ferritins. Generally, ferrihydrite [19] forms at the early stage of biomineralization process. Although ferrihydrite is a labile form of crystal, it is present in the ferritin due to its ability to demineralize faster than the other forms of iron oxide.[36] From thermodynamic standpoint, formation of hematite is favoured from the ferrihydrite crystal structure.[41,42] However, the inner environment and the protein chemistry tend to retain the water molecules and influences the formation of selective crystal types.[36] In addition to ferrihydrite and hematite, traces of magnetite phase was also observed in hydrated HSF, which was not evident in HHF. Although the *d* spacings can be matched with two different iron oxide types, it can be speculated that the crystal structure is closer to magnetite as the EELS results also indicated the higher ratios of Fe^{2+}/Fe^{3+} in HSF. The presence of magnetite in ferritin has also been supported by several electron microscopy[3,8,9,23] and non-EM[23,25–27,1] based experiments. Further, a model for magnetization of ferritin[28] supported the presence of magnetite in ferritins. Biologically, the presence of magnetite could be related to the oxidation and precipitation of adsorbed ferrous ions on the surface of ferrihydrite crystal core.[48] The diffraction patterns of wet HHF collected from different areas indicated the presence of magnetite or maghemite in addition to ferrihydrite and hematite. The EELS studies indicated higher ratios of Fe^{3+}/ Fe^{2+} in comparison with HSF, because of which there is a higher probability of having maghemite instead of magnetite in HHF.

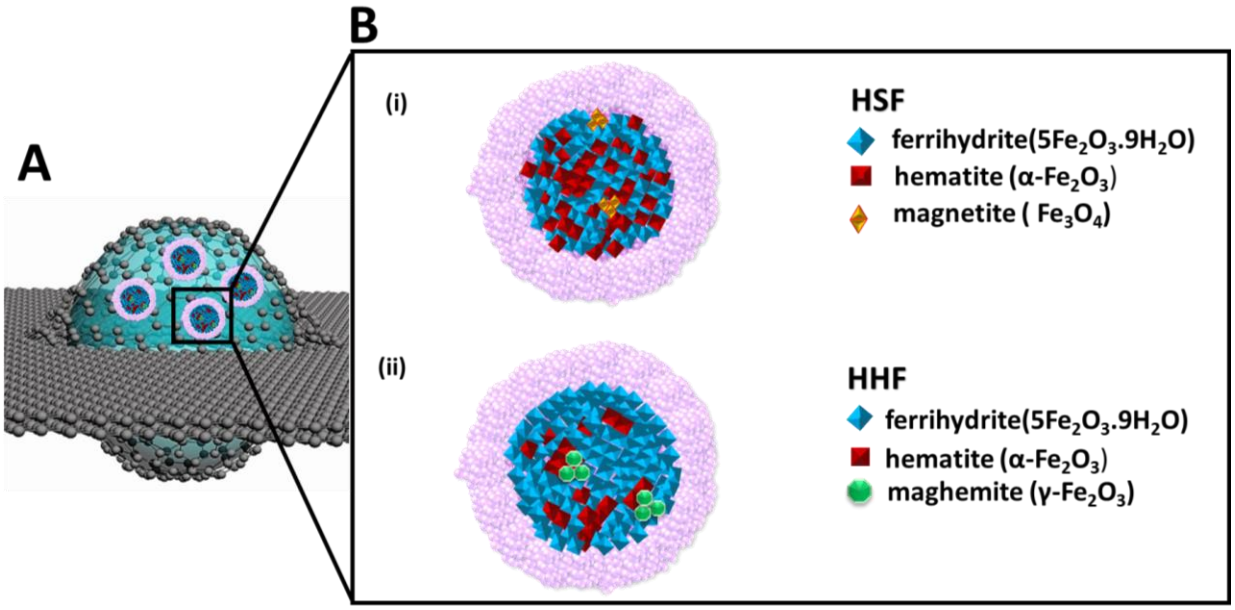

Scheme 1: The schematic shows the encapsulation of ferritin proteins within GLC capsules and the differences in the iron oxide phases of HSF and HHF. **A**. graphene liquid cell encapsulation allows imaging of ferritin proteins in their native liquid state. (**B**-i) HSF protein with the protein shell (pink color) and the iron mineral core composed of ferrihydrite (Fh), hematite (H), and the traces of magnetite (M). The percentage composition and location of Fh, H, and M are represented solely for schematic purpose. (**B**-ii) HHF protein with the iron mineral core composed of ferrihydrite (Fh), hematite (H) and maghemite (MH). The percentage composition and distribution of Fh, H, and MH are represented solely for schematic purpose.

While it is less likely that the observation of magnetite in wet state to be due to the effect of electron beam radiation since the same phenomenon was not observed in dry state ferritins, we believe further studies on the role of electron beam on this phenomenon are necessary. It is interesting to note that the type of iron

oxides formed inside the protein shells are limited to the above-mentioned types. However in the absence of protein shell, formation of akaganeite (β-FeO(OH)[49], goethite (γ-FeO(OH)) and lepidocrocite (α –FeO(OH))[36] are favoured based on the classical nucleation theory. The surface energy due the larger surface to volume ratio of the mineral core can contribute to the thermodynamic stability of the nanosized crystals.[36]

GLC-STEM-EELS white line analysis showed higher ratio of Fe/O, thus higher Fe^{3+}/ Fe^{2+} in HHF compared to the HSF. This observation could be due to several possibilities: (1) The ability of HSF to apprehend higher numbers of Fe^{2+} compared to HHF[35] could result in the nucleation of iron ions before the completion of iron oxidation from Fe^{2+} to Fe^{3+} form. (2) The metabolic state of the cells in the different organs[50]. (3) The presence of larger ratios of H/L subunits in HHF compared to HSF could affect the ratio of Fe^{3+}/Fe^{2+}.[35] After the ferrous iron internalization by ferritin through eight hydrophilic channels, the dinuclear ferroxidase sites, which are present in H subunits convert ferrous iron to ferric oxide species through $2Fe^{2+}+O_2 \rightarrow Fe^{3+}$-O-O-$Fe^{3+}$.

It should be noted that, this is the first time, the structural and chemical characterization of hydrated HSF and HHF are reported. There are some SAED and EELS studies that report the differences in H and L rich ferritins based on the conventional sample preparation for TEM studies (no cryoTEM).[4,8,9,51] However, there are discrepancies in the results that are previously reported. While some of the studies report that both H- and L- rich ferritins are composed of ferrihydrite[51,9] , there are also results which supports the polyphasic nature of iron oxides.[8,4] Our results indicate that both HSF and HHF are polyphasic in nature, with iron oxide composites. While drying of the proteins are not desirable (in c-TEM), it is also possible that proteins are the victim of electron induced radiolysis in absence of protective graphene cover. Studies have shown that biological samples with protective graphene cover were less prone to radiolysis even with higher total dose compared to threshold dose[30,18,52]. It should also be noted that presence of buffers surrounding the protein might influence the pH of the solution by establishing an equilibrium between oxidation and reduction process.[53,54] While it is possible to have the effect of buffer in the liquid environment, it becomes challenging to maintain the buffers during dry c-TEM imaging. This could possibly differentiate the results obtained via the c-TEM versus the observation made via our GLC-TEM. It would be interesting to study the influence of solvents in the solution in maintaining an exceptionally high stability towards electron beam induced iron transformations. This could possibly differentiate the results obtained via the c-TEM versus the observation made via our GLC-TEM.

Considering the need for surrounding liquid environment to keep the protein structure intact,[55] the crystal structure and chemistry of HSF and HHF were evaluated in liquid state. Further, to understand the differences in composition of the protein in native wet environment and the dry state results reported in literature [16,9], same analysis was also carried out in absence of liquid. The results obtained from the dry state ferritin indicated the predominant hematite phase with some ferrihydrite[4], in addition to the traces of goethite or magnetite (Figure S1). It is reported that the loss of water favours the formation of hematite[42] which might be a reason to observe major phases of hematite in dry state diffraction studies. Further, magnetite was observed only in wet state HHF diffraction analysis. It should be noted that, there has been also a lack of characterization studies on the iron oxide mineral type in the HHF core in literature, thus, the comparison of the wet and dry results with the dry state reports from literature was limited to HSF. To comprehend the differences between dry and wet state in terms of O to Fe ratio, EELS was also carried out in both states and it was observed that the ratio in wet state HSF is higher than dry state HSF (Figure S2). In addition to that, a sharp pre edge feature at 709.2eV and the edge at 710.7eV with a difference of 1.5eV was observed in the dry state which can be inferred as hematite.[56] The pre edge was not prominent in wet state which might be due to the scant amount of hematite in wet state compared to dry condition. The ferritin structure in dry state might not be a true representation because of the TEM sample preparation techniques that can cause deviations from native properties of biological samples. The loss of liquid after drop casting onto TEM grid and further drying of the sample in the electron microscope chamber could be an additional factor affecting the protein structure. The role of graphene to keep the liquid layer intact around the protein shell has an impact on the integrity of the proteins. The hydrogen bonds hold the polypeptide bundles together in presence of water and thus might have an impact on the iron oxides formed inside the protein. In absence of water, the hydrogen bonds break down and the structural integrity of the protein shell surrounding the iron oxide core is lost.[55] Hence, the loss of protein will remove some of the contribution of oxygen from the shell, decreasing O/Fe ratio, thus, Fe^{3+}/Fe^{2+} ratio. While we noted the differences in L_3/L_2 ratio edges in wet and dry specimens, there is small overlap pointing to the

fact that statistical analysis should be performed on large datasets to fully analyze the trend in L_3/L_2 ratio in wet and dry states

We should also highlight that studying proteins in liquid state has some advantages over the cryo-TEM technique: (1) Due to the ability to keep the liquid surrounding the protein as one of the active components, the hydration forces of water at room temperature helps maintain the stability of the proteins.[57] On the other hand, the cryo freezing of water not only increases the density of the protein artificially, but also impacts the inner cavity causing protein destabilization.[58] Studying proteins in liquid at room temperature will facilitate the protein stability. (2) Additionally, liquid-cell TEM allows the study of dynamics or structural transformation in proteins. (3) Furthermore, the GLC-TEM technique does not require costly cryo-TEM instrumentation or special TEM holders.

The effect of electron dose on the chemistry of the ferritin was also considered in this study. The electron dose was rigorously controlled during imaging to minimize the effect of electron beam on determining the type of iron oxide crystal in ferritin cores. In fact, our earlier work has shown the strategy to control the chemical environment of GLCs.[29] The concentration of H_2 species during the electron beam irradiation is dependent on the electron dose rate(Figure S3 and Video S1).[59] The relationship can be given by the equation: $C_{H_2} = \alpha_i \, (10^5 . S \, . D_r \,)^{\beta i}$, where C_{H_2} is the concentration of hydrogen species, S is the stopping power, α_i and β_i are constants , and D_r is the dose rate.[59] With lower electron dose rate, the bubble formation and the generation of radiolysis species can be controlled as also reported by Wang *et al*. [29] This is because, the radiolysis products increase exponentially at the onset of electron beam irradiation. However, an equilibrium is established over time due to the annihilation reaction between the primary radiolysis products and water.[29] This effect establishes a direct relationship between electron dose rate and the formation of radiolysis products.[29] Future studies should incorporate the effect of dose vs dose rate while studying the iron oxides in ferritin.

Further, in the same work, it was shown that the internal pressure in the GLCs have a direct correlation with the threshold electron dose rate, given by the relation $p^2 \, \alpha \, D_r$; where p is the pressure and D_r is the electron dose rate. [29] The experiments were designed taking the effect of electron dose rate into consideration (as also demonstrated in Figure S4 and S5). The electron dose calculation and the corresponding doses for different imaging and EELS experiments are reported in the experimental section. While the electron dose induced radiolysis products can influence the local environment facilitating the iron reduction process, it should be noted that besides protective graphene cover, the proteins are surrounded by the buffered solution at pH 7.5. Studies have shown the influence of both the initial pH as well as the buffers affecting the local environment of the solution[53]. In deionized water, the effect of radiolysis species such as H_3O^+ ions are known to decrease the pH of the solution, thus influencing a reducing environment[53]. However, in presence of buffered solution containing chloride ions, there is a possibility that the condition is reversed, favoring an equilibrium state between oxidation and reduction processes.[54] However the effect of preservatives such as bromo-nitro-dioxanes and methylsothiazolone are not well studied. It would be interesting to study the effect of these species in the electron beam-induced transformations.

Pan and his coworkers[10] studied the composition of ferritin subjected to varied electron doses starting from the 10^5 to 10^9 electrons/nm^2 electron dose in dry state. They also reported that Fe^{3+}/Fe^{2+} ratio of iron in hemosiderin and cytosolic ferritins (which was studied in this work as well) did not vary with the increase of total electron dose[10]. In our study, although the dose conditions were the same in both the types of ferritins, the chemical information obtained from HSF and HHF proteins were different indicating that the conclusions in this study are not influenced by the electron beam. The ability of using higher electron doses during GLC imaging compared other low dose electron imaging setups could be attributed to the novel material properties of graphene: (i) Graphene is a very good electronic conductor, eliminating further accumulation of incident electrons in the sample during electron imaging. Hence, sample charging and resulting formation of radiolysis products were minimized.[60] (ii) Due to the lower total thickness of GLCs, number of secondary electron formed due to electron-sample interaction is lower than the relatively thicker Si_3N_4 based fluid cell setup.[61] (iii) In the event of radiolysis, the radicals form and graphene is also reported to be good radical scavenger, which helps in the prevention of possible unwanted radical-sample interaction (also see Supplementary Information).[30] Due to these reasons, GLCs enables the utilization of higher electron doses in comparison to conventional TEM imaging of biological or beam-sensitive samples.

Conclusion

Graphene liquid cell-TEM imaging and spectroscopy were utilized to analyse the structural and chemical differences in the iron oxide cores of different organ ferritins. It is expected that the higher number of active sites in H subunits facilitate continuous oxidation and rapid biomineralization of iron oxides. Both HSF and HHF were observed to have ferrihydrite and hematite. However, the L- and H subunit rich ferritins also showed traces of magnetite and maghemite, respectively. Excess of iron ions that enter the protein might deposit on the surface of iron core crystal resulting in the magnetite formation. Slow kinetics and incomplete biomineralization could also be another reason for the observation of the magnetite in HSF and the higher rate of reduction process can explain the observation of maghemite in HHF. Higher ratios of O/Fe or Fe^{3+}/ Fe^{2+} was observed in HHF compared to HSF in liquid state. This might be due to several factors which includes the number of iron ions that are available for oxidation, the metabolic state of the cells in the organ, as well as the presence of larger ratios of H/L subunits causing ferroxidation in HHFs compared to HSFs. Future studies can focus on observing the biomineralization in real-time, which can further help understand the correlation between the different iron oxides chemical composition and the organ ferritins. It was also observed from the dried HSF contained lower ratio of Fe^{3+}/ Fe^{2+} as compared to the wet HSF. This is attributed to the degraded nature of air-dried ferritin resulting in the loss of oxygen from ferritin shell that contributes to the Fe/O ratio. It should be noted that this study was limited to characterization of crystalline iron oxides in HSF and HHF. Future studies should be considered to study the non-crystalline or partially crystalline forms of iron oxide in ferritin. The ability of GLC-TEM to image proteins in native wet condition offers new opportunities in exploring the interaction of proteins and inorganic materials. Future directions will focus on observing the iron core growth and understanding the nucleation mechanism in ferritin using the *in-situ* liquid microscopy.

Experimental Procedure

Materials

HSF (Catalog # 270-50) and HHF (Catalog #FERT16-R-50) were purchased from Lee Biosolutions, USA and Alpha Diagnostics International, USA respectively. The protein samples were diluted with 1X PBS buffer to 0.4mg/ml for all the experiments.

Graphene Grids

The grids used for the experiments are 300 mesh Au lacey carbon TEM grids (LC325) purchased from Electron Microscopy Sciences (EMS). A slightly modified protocol was followed from Regan and his coauthors.[62] The gold grids were placed on the in-house grown graphene coated copper sheets. The grids and the copper sheets were flattened and pressed against each other by applying gentle pressure through the lens paper. Further, 1µl of IPA was added to the sides of the grid to attach the grid to the copper sheet. The gold grids on the copper sheet were air dried for 5 minutes to get rid of excess IPA. Then the grids were placed on the hot plate at 50°C for 10 minutes. The copper sheet was placed in the $FeCl_3$ etchant for 3 hours. To prevent the silicon nanoparticles that would deposit from the silicon-based glass containers during etching, Nalgene containers were used for all the experiments. After 3 hours, the grids were washed with deionized water for three times.

TEM Sample Preparation

The protein samples were drop-casted in the commercially available lacey carbon film coated copper grid (Catalog# LC300-CU, Electron Microscopy Sciences) and air-dried to collect the HR-TEM and SAED patterns. Further, the liquid protein samples were encapsulated in the graphene sandwiches as described by Wang *et al*, 2014[18] for STEM images and chemical characterization using the STEM- EELS.

Sample Characterization

STEM images were collected from GLC-TEM experiments and were processed with ImageJ to determine the size and morphology of the particles. The analysis was done for 70 different particles for each ferritin sample. The particle sizes were grouped with the bins of $5nm^2$. Then, the average area was calculated along with the frequency. To this end, the data set was plotted in Origin Pro (version: b9.4.0.220). The structural characterization of both the samples were analysed by measuring the interplanar distances in both GLC and dry state were carried out via 80kV Hitachi HT7700 at 80kV and JEOL 3010 at 300kV, respectively. HR-TEM images on the dry samples were collected using JEOL-JEM 3010 at 300kV. GLC-TEM electron imaging and diffraction were collected with 1 second exposure using the electron dose range of 16 to 181 $e/Å^2$. Dry state TEM imaging and diffraction were collected with 0.1 second exposure. GLC-HAADF STEM imaging and chemical characterization were carried out using the probe aberration corrected JEOL-JEM 200CF operated at 80keV. The microscope is equipped with Cold Field Emission Gun and GIF Quantum EELS (Gatan, Inc., USA) that has spatial resolution of 1.3 Å and energy

resolution of about 0.35eV. For STEM imaging and EELS, a convergence semi angle of 22 and 17.8 mrad was used, respectively. For STEM images, HAADF detector with inner detection angle of 90 mrad was used for better Z contrast. Images were collected with 512 X 512 pixels and dwell time of 31.2 µs. The video was collected in Ronchigram mode with 0.01 s per frame exposure time. For EELS, a collection angle of 53.4 mrad was used for better quality signal. The energy resolution was determined by measuring the full width half maximum of the zero-loss peak and it was around 0.6 eV. The spectrum was acquired with the dispersion of 0.15 eV/channel with exposure time of 0.1s. The electron dose rate for HAADF imaging and EELS analysis were approximately 9 e/Å^2 /s and 7.2x10^6 e/Å^2/s, respectively. Origin Pro[18] was used to calculate the integral white line intensities.

Data Analysis

The interplanar distances were measured both via the FFT of the image in HR-TEM images and SAED patterns using Digital Micrograph. SAED data was analysed using the Digital Micrograph. For the EELS analysis, the background was subtracted using the 50eV integration window in the Digital Micrograph and the energy range was considered from 705-730 eV for the analysis.[63] The L_3 and the L_2 edges were normalized and the background was subtracted for plural scattering. Then, the related area integral ratio was calculated by fitting a gaussian under the peaks using the Origin Pro (version: b9.4.0.220).[40] Comparison figure of individual magnetite standard, HSF, HHF, and hematite standard EELS spectra was reported after 3 channel spectrum averaging.

Conflict of Interest:

The authors declare no conflict of interest.

Acknowledgements

This work is funded by National Science Foundation CAREER award (DMR-1564950). R. Shahbazian-Yassar's contribution is supported by NSF DMR-1710049. This work made use of instruments in the Electron Microscopy Core of UIC's Research Resources Centre. The UIC JEOL JEM-ARM200CF is supported by an MRI-R2 grant from the National Science Foundation (Grant No. DMR-0959470*)*. The authors acknowledge UIC Research Resource Centre for providing the instrumental support. GLC SAED work made use of the EPIC facility of Northwestern University's NU*ANCE* Centre, which has received support from the Soft and Hybrid Nanotechnology Experimental (SHyNE) Resource (NSF ECCS-1542205); the MRSEC program (NSF DMR-1720139) at the Materials Research Centre; the International Institute for Nanotechnology (IIN); the Keck Foundation; and the State of Illinois, through the IIN.

References:

1. Harrison PM, A. P. The ferritins: molecular properties, iron storage function and cellular regulation. *Biochim Biophys Acta ;* **1275:161–2**, (1996).

2. Harrison, P. M., Fischbach, F. A., Hoy, T. G. & Haggis, G. H. Ferric oxyhydroxide core of ferritin. *Nature* **216**, 1188–1190 (1967).

3. Williams, J. M., Danson, D. P. & Janot, C. A Mossbauer determination of the iron core particle size distribution in ferritin. *Phys. Med. Biol.* **23**, 001 (1978).

4. Galvez, N. *et al.* Comparative structural and chemical studies of ferritin cores with gradual removal of their iron contents. *J. Am. Chem. Soc.* **130**, 8062–8068 (2008).

5. Hwang, J. *et al.* A short Fe-Fe distance in peroxodiferric ferritin: control of Fe substrate versus cofactor decay? *Science* **287**, 122–5 (2000).

6. Smith, D. J. Ultimate resolution in the electron microscope? *Mater. Today* **11**, 30–38 (2008).

7. Muir, A. R. The molecular structure of isolated and intracellular ferritin. *Q. J. Exp. Physiol. Cogn. Med. Sci.* **45**, 192–201 (1960).

8. Quintana, C., Cowley, J. M. & Marhic, C. Electron nanodiffraction and high-resolution electron microscopy studies of the structure and composition of physiological and pathological ferritin. *J. Struct. Biol.* **147**, 166–178 (2004).

9. Pan, Y. H. *et al.* 3D morphology of the human hepatic ferritin mineral core: New evidence for a subunit structure revealed by single particle analysis of HAADF-STEM images. *J. Struct. Biol.* **166**, 22–31 (2009).

10. Pan, Y. H. *et al.* Electron-beam-induced reduction of Fe3+ in iron phosphate dihydrate, ferrihydrite, haemosiderin and ferritin as revealed by electron energy-loss spectroscopy. *Ultramicroscopy* **110**, 1020–1032 (2010).

11. Farrant, J. L. L. AN Electron Microscopic Study of Ferritin. *Biochim. Biophys. Acta* **13**, 569–576 (1937).

12. Massover, W. H. & Cowley, J. M. The Ultrastructure of Ferritin Macromolecules. The Lattice Structure of the Core Crystallites. *Proc. Natl. Acad. Sci.* **70**, 3847–3851 (1973).

13. Cowley, J. M., Janney, D. E., Gerkin, R. C. & Buseck, P. R. The structure of ferritin cores determined by electron nanodiffraction. *J. Struct. Biol.* **131**, 210–6 (2000).

14. Quintana, C. *et al.* Initial studies with high resolution TEM and electron energy loss spectroscopy studies of ferritin cores extracted from brains of patients with progressive supranuclear palsy and Alzheimer disease. *Cell. Mol. Biol.* **46**, 807–820 (2000).

15. Quintana, C., Bonnet, N., Jeantet, A. Y. & Chemelle, P. Crystallographic study of the ferritin molecule: new results obtained from natural crystals in situ (mollusc oocyte) and from isolated molecules (horse spleen). *Biol. Cell* **59**, 247–254 (1987).

16. Pan, Y. *et al.* Electron beam damage studies of synthetic 6-line ferrihydrite and ferritin molecule cores within a human liver biopsy. *Micron* **37**, 403–411 (2006).

17. Calvert, C. C., Brown, A. & Brydson, R. Determination of the local chemistry of iron in inorganic and organic materials. *J. Electron Spectros. Relat. Phenomena* **143**, 173–187 (2005).

18. Wang, C., Qiao, Q., Shokuhfar, T. & Klie, R. F. High-resolution electron microscopy and spectroscopy of ferritin in biocompatible graphene liquid cells and graphene sandwiches. *Adv. Mater.* **26**, 3410–3414 (2014).

19. Massover, W. H. Ultrastructure of ferritin and apoferritin: A review. *Micron* **24**, 389–437 (1993).

20. Jonge, N. D. and F. M. R. Electron microscopy of specimens in liquid. *Nat. Nanotechnol.* **6**, (2011).

21. Peckys, D. B. & De Jonge, N. Visualizing gold nanoparticle uptake in live cells with liquid scanning transmission electron microscopy. *Nano Lett.* **11**, 1733–1738 (2011).

22. Murai, T. *et al.* Low Cholesterol Triggers Membrane Microdomain-dependent CD44 Shedding and Suppresses Tumor Cell Migration. *J. Biol. Chem.* **286**, 1999–2007 (2011).

23. Peckys, D. B., Mazur, P., Gould, K. L. & De Jonge, N. Fully hydrated yeast cells imaged with electron microscopy. *Biophys. J.* **100**, 2522–2529 (2011).

24. Hoppe, S. M., Sasaki, D. Y., Kinghorn, A. N. & Hattar, K. In-Situ Transmission Electron Microscopy of Liposomes in an Aqueous Environment. *Langmuir* **29**, 9958–9961 (2013).

25. Kennedy, E., Nelson, E. M., Tanaka, T., Damiano, J. & Timp, G. Live Bacterial Physiology Visualized with 5 nm Resolution Using Scanning Transmission Electron Microscopy. *ACS Nano* **10**, 2669–2677 (2016).

26. Evans, J. E. & Browning, N. D. Enabling direct nanoscale observations of biological reactions with dynamic TEM. *Journal of Electron Microscopy* **62**, 147–156 (2013).

27. Evans, J. E. *et al.* Visualizing macromolecular complexes with in situ liquid scanning transmission electron microscopy. *Micron* **43**, 1085–1090 (2012).

28. Yuk, J. M. *et al.* High-Resolution Em of Colloidal Nanocrystal Growth Using Graphene Liquid Cells. *Science (80-.).* **336**, 61–64 (2012).

29. Wang, C., Shokuhfar, T. & Klie, R. F. Precise In Situ Modulation of Local Liquid Chemistry via Electron Irradiation in Nanoreactors Based on Graphene Liquid Cells. *Adv. Mater.* **28**, 7716–7722 (2016).

30. Cho, H. *et al.* The Use of Graphene and Its Derivatives for Liquid-Phase Transmission Electron Microscopy of Radiation-Sensitive Specimens. *Nano Lett.* **17**, 414–420 (2017).

31. López-Castro, J. D. *et al.* A new approach to the ferritin iron core growth: influence of the H/L ratio on the core shape. *Dalton Trans.* **41**, 1320–4 (2012).

32. Ford, G. C. *et al.* Ferritin: Design and Formation of an Iron-Storage Molecule. *Philos. Trans. R. Soc. B Biol. Sci.* **304**, 551–565 (1984).

33. Fischbach, F. A., Harrison, P. M. & Hoy, T. G. The structural relationship between ferritin protein and its mineral core. *J. Mol. Biol.* **39**, 235–8 (1969).

34. Jian, N., Dowle, M., Horniblow, R. D., Tselepis, C. & Palmer, R. E. Morphology of the ferritin iron core by aberration corrected scanning transmission electron microscopy. *Nanotechnology* **27**, (2016).

35. Mehlenbacher, M. *et al.* Iron Oxidation and Core Formation in Recombinant Heteropolymeric Human Ferritins. *Biochemistry* **56**, 3900–3912 (2017).

36. Chasteen, N. D. & Harrison, P. M. Mineralization in ferritin: an efficient means of iron storage. *J. Struct. Biol.* **126**, 182–194 (1999).

37. Cornell, R. M. & Schwertmann, U. *The Iron Oxides: Structure, Properties, Reactions, Occurrences and Uses*. (Wiley, 2006).

38. Lajaunie, L., Boucher, F., Dessapt, R. & Moreau, P. Quantitative use of electron energy-loss spectroscopy Mo-M2,3 edges for the study of molybdenum oxides. *Ultramicroscopy* **149**, 1–8 (2015).

39. Sparrow T.G., Williams B. G., Rao C.N.R., T. J. M. L3/L2 White Line Intensity Ratios in the Electron Energy- Loss Spectra of 3d Transition Metal Oxides. *Chem. Phys. Lett.* **108**, 547–550 (1984).

40. Graetz, J., Ahn, C. C., Ouyang, H., Rez, P. & Fultz, B. White lines and d-band occupancy for the 3d transition-metal oxides and lithium transition-metal oxides. *Phys. Rev. B, 2004, 69,235103* **69**, (2004).

41. Das, S., Hendry, M. J. & Essilfie-Dughan, J. Transformation of Two-Line Ferrihydrite to Goethite and Hematite as a Function of pH and Temperature. *Environ. Sci. Technol.* **45**, 268–275 (2011).

42. Schwertmann, U., Friedl, J. & Stanjek, H. From Fe(III) ions to ferrihydrite and then to hematite. *J. Colloid Interface Sci.* **209**, 215–223 (1999).

43. Quintana, C. *et al.* Study of the localization of iron, ferritin, and hemosiderin in Alzheimer's disease hippocampus by analytical microscopy at the subcellular level. *J. Struct. Biol.* **153**, 42–54 (2006).

44. Gossuin, Y., Muller, R. N. & Gillis, P. Relaxation induced by ferritin: A better understanding for an improved MRI iron quantification. *NMR in Biomedicine* **17**, 427–432 (2004).

45. Yurtaeva, S. V. *et al.* Magnetic Resonance of Ferritin Crystalline Particles in Tumor Tissue. *Appl. Magn. Reson.* **42**, 299–311 (2012).

46. Koralewski, M. *et al.* Magnetic birefringence study of the magnetic core structure of ferritin. in *Acta Physica Polonica A* **121**, 1237–1239 (2012).

47. Brem, F., Stamm, G. & Hirt, A. M. Modeling the magnetic behavior of horse spleen ferritin with a two-phase core structure. *J. Appl. Phys.* **99**, 123906 (2006).

48. Yang, L., Steefel, C. I., Marcus, M. A. & Bargar, J. R. Kinetics of Fe(II)-catalyzed transformation of 6-line ferrihydrite under anaerobic flow conditions. *Environ. Sci. Technol.* **44**, 5469–5475 (2010).

49. De Yoreo, J. J. In-situ liquid phase TEM observations of nucleation and growth processes. *Progress in Crystal Growth and Characterization of Materials* **62**, 69–88 (2016).

50. Goto, Y., Paterson, M. & Listowsky, I. Iron uptake and regulation of ferritin synthesis by hepatoma cells in hormone-supplemented serum-free media. *J. Biol. Chem.* **258**, 5248–5255 (1983).

51. Wade, V. J. *et al.* Influence of site-directed modifications on the formation of iron cores in ferritin. *J. Mol. Biol.* **221**, 1443–1452 (1991).

52. Park, J. *et al.* Direct Observation of Wet Biological Samples by Graphene Liquid Cell Transmission Electron Microscopy. *Nano Lett.* **15**, 4737–4744 (2015).

53. Wang, X., Yang, J., Andrei, C. M., Soleymani, L. & Grandfield, K. Biomineralization of calcium phosphate revealed by in situ liquid-phase electron microscopy. *Commun. Chem.* **1**, 80 (2018).

54. Hermannsdörfer, J., De Jonge, N. & Verch, A. Electron beam induced chemistry of gold nanoparticles in saline solution. *Chem. Commun.* **51**, 16393–16396 (2015).

55. Haider, K., Wickstrom, L., Ramsey, S., Gilson, M. K. & Kurtzman, T. Enthalpic Breakdown of Water Structure on Protein Active-Site Surfaces. *J. Phys. Chem. B* **120**, 8743–8756 (2016).

56. Paterson, J. H. & Krivanek, O. L. Elnes of 3d transition-metal oxides. *Ultramicroscopy* **32**, 319–325 (1990).

57. Levy, Y. & Onuchic, J. N. Water Mediation in Protein Folding and Molecular Recognition. in *Annual Review of Biophysics and Biomolecular Structure* **35**, 389–415 (2006).

58. Halle, B. Biomolecular cryocrystallography: Structural changes during flash-cooling. *Proc. Natl. Acad. Sci.* **101**, 4793–4798 (2004).

59. Schneider, N. M. *et al.* Electron-Water interactions and implications for liquid cell electron microscopy. *J. Phys. Chem. C* **118**, 22373–22382 (2014).

60. Bansal, R. K., Monroe, G. E., Dahan, R., El Gharras, O. & Bahri, A. High-Resolution EM of Colloidal Nanocrystal Growth Using Graphene Liquid Cells.

10, 641–646 (1994).

61. Park, J., Adiga, V. P., Zettl, A., Paul Alivisatos, A. & Alivisatos, A. P. High Resolution Imaging in the Graphene Liquid Cell. in *F.Ross (Ed.), Liquid Cell Electron Microscopy (Advances in Microscopy and Microanalysis)* 393–407 (Cambridge University Press, 2016). doi:10.1017/9781316337455.020

62. Regan, W. *et al.* A direct transfer of layer-area graphene. *Appl. Phys. Lett.* **96**, 2008–2011 (2010).

63. Garvie, L. A. J. & Buseck, P. R. Ratios of ferrous to ferric iron from nanometre-sized areas in minerals. *Nature* **396**, 667–670 (1998).

Journal Name

ARTICLE